# Multiport Bidirectional SRM Drives for Solar-Assisted Hybrid Electric Bus Powertrain With Flexible Driving and Self-Charging Functions

Chun Gan, *Member, IEEE*, Nan Jin, *Member, IEEE*, Qingguo Sun, Wubin Kong, *Member, IEEE*, Yihua Hu, *Senior Member, IEEE*, and Leon M. Tolbert, *Fellow, IEEE*

***Abstract*—Hybrid electric bus (HEB) presents an emerging solution to exhaust gas emissions in urban transport. This paper proposes a multiport bidirectional switched reluctance motor (SRM) drive for solar-assisted HEB (SHEB) powertrain, which not only improves the motoring performance, but also achieves flexible charging functions. To extend the driving miles and achieve self-charging ability, photovoltaic (PV) panels are installed on the bus to decrease the reliance on fuels/batteries and charging stations. A bidirectional front-end circuit with a PV-fed circuit is designed to integrate electrical components into one converter. Six driving and five charging modes are achieved. The dc voltage is boosted by the battery in generator control unit (GCU) driving mode and by the charge capacitor in battery driving mode, where the torque capability is improved. Usually, an extra converter is needed to achieve battery charging. In this paper, the battery can be directly charged by the demagnetization current in GCU or PV driving mode, and can be quickly charged by the PV panels and GCU/AC grids at SHEB standstill conditions, by utilizing the traction motor windings and integrated converter circuit, without external charging converters. Experiments on a three-phase 12/8 SRM confirm the effectiveness of the proposed drive and control scheme.**

***Index Terms*—Solar hybrid electric bus (SHEB), multiport bidirectional converter, photovoltaics (PV), boosted dc voltage, switched reluctance motor (SRM).**

## I. INTRODUCTION

Owing to the high demand of fuel efficiency and environment protection against air pollution, hybrid electric buses (HEBs) have received much attention for urban transportations [1]-[6]. For electric powertrain systems, permanent-magnet synchronous machines (PMSMs) are a popular solution because of their high efficiency and high torque density [7]-[9]. However, PMSMs need to use permanent magnets, which bring about problems of high cost and poor stability. Therefore, many efforts are focusing on developing rare-earth-less or rare-earth-free motors for future traction drives [10]-[12]. Switched reluctance motor (SRM) has received significant interest for electric vehicles [13]-[21], which has no rotor windings and permanent magnets. SRMs have the advantages of robust structure, low cost, high reliability, wide-speed range, and good fault tolerance ability, which give these motors the ability to work in high-speed, high-temperature, and safety-critical applications.

Some advanced converter topologies have been reported for SRMs to improve the system performance [22]-[33]. SRM driving by three-phase standard inverters has been presented in [22]-[24], and control strategies are put forward accordingly. In order to increase the torque capability, converters with boosted dc-link voltage are proposed for SRMs [25]-[30]. A quasi-three-level converter is developed in [25], to reduce the current rising and falling times. However, twice as many power transistors as traditional converters should be used. In [26], a single-phase SRM drive with high demagnetization voltage is presented by employing additional inductors, which reduce the efficiency and power density. In [27], a dual voltage converter is put forward with higher voltages across the machine windings, while four capacitors are needed. Multilevel converters by using two charge capacitors are developed in [28]-[30] to boost the dc voltage for high-speed operations. A low-cost battery-powered two-phase SRM drive is presented in [31], and the battery charging is directly achieved by utilizing SRM windings, without additional inductors and charging units. A new dual voltage SRM drive is proposed to allow motoring from the battery and AC source, where the battery charging function is integrated into the motor drive [32]. A quasi-Z-source integrated multiport converter is designed for SRMs in [33], to reduce the dc-link capacitance, boost the dc voltage, and enable wide-speed operation.

For electric vehicles, state-of-the-art SRM drives have been presented in [34]-[40] to achieve integrated driving and charging functions. A dc/dc converter is employed for battery powered SRM drives to improve the dc voltage and speed dynamic responses [34], while the additional use of inductors and capacitors reduces the power density. An integrated driving/charging SRM drive is presented for pure

Manuscript received July 10, 2017; revised October 5, 2017; accepted November 29, 2017. This work was supported in part by the National Nature Science Foundation of China (51607159, U1604136), and in part by the Scientific and Technological Innovation Talents Project in Henan Province (18HASTIT025, 172102410068). *(Corresponding author: Nan Jin.)*

C. Gan is with the Department of Electrical Engineering and Computer Science, University of Tennessee, Knoxville, TN 37996, USA, and also with the College of Electrical Engineering, Zhejiang University, Hangzhou 310027, China (e-mail: cgan@utk.edu).

N. Jin is with the College of Electric and Information Engineering, Zhengzhou University of Light Industry, Zhengzhou 450002, China, and also with the Department of Electrical Engineering and Computer Science, University of Tennessee, Knoxville, TN 37996, USA (e-mail: njin3@utk.edu).

Q. Sun is with the College of Electrical Engineering, Zhejiang University, Hangzhou 310027, China (e-mail: lwsunqg@163.com).

W. Kong is with the School of Electrical and Electronic Engineering, Huazhong University of Science and Technology, Wuhan 430074, China (e-mail: wubinkong@126.com).

Y. Hu is with the Department of Electronic and Electrical Engineering, University of Liverpool, Liverpool, U.K. (e-mail: y.hu35@liverpool.ac.uk).

L. M. Tolbert is with the Department of Electrical Engineering and Computer Science, University of Tennessee, Knoxville, TN 37996, USA (e-mail: tolbert@utk.edu).

battery-powered vehicles in [35]. Three-phase intelligent power modules are used in a modified Miller converter, which is not equipped with fault-tolerance ability. In [36], an SRM drive with a front-end dc/dc converter is presented and control schemes are also developed with flexible charging functions and excellent motoring performance. An improved SRM drive derived from a C-dump converter is proposed for hybrid vehicles with grid charging capability [37]. However, the fault-tolerance ability is poor due to non-isolated phases in the circuit, and the boosted dc voltage cannot be achieved. In [38], a split converter topology is proposed for four-phase SRM-based pure battery-powered vehicles to achieve flexible battery charging functions, where the midpoints of the phase windings are connected. However, conventional winding connections need to be changed, which cannot be used for three-phase SRM drives. To restrain the current ripple and improve the motoring performance, a three-port converter is put forward in [39] for battery-powered SRM drives in electric vehicle applications. In [40], an integrated SRM converter for plug-in hybrid vehicles is developed. Although integrated functions are obtained, multiple ports and self-charging ability are not achieved, which leads to a high demand for batteries/fuels and also charging stations.

However, to popularize HEBs in an urban environment, a large number of charging stations are required. It is clear that the construction costs are considerable if existing internal combustion engine (ICE)-based buses are replaced by new electrified ones. There is also another issue related to HEBs in that the possible driving distance is short in pure battery-powered mode, due to the limitation of current battery technologies. Therefore, to overcome these issues, photovoltaic (PV) panels can be employed to assist the main power source in driving mode and achieve battery charging, which will considerably reduce the reliance on fuels, batteries, and charging stations. Nowadays, PV panels have been employed in electrified transport and aircraft applications [41]-[44]. For SRMs, a PV integrated converter is presented in [45]. However, all three phases share one chopping switch, and bidirectional multiport topology is not achieved, which leads to poor fault-tolerance ability and control flexibility.

Therefore, in order to achieve multi-source operation, improve the motoring performance, and obtain flexible self-charging functions, this paper presents a multiport bidirectional SRM drive for solar-assisted HEB (SHEB) applications. A bidirectional front-end circuit is designed to combine the asymmetrical half-bridge converter for integrated functions. PV panels are employed as an assisted sustainable energy source to extend the driving range and reduce the reliance on charging stations. Multiple driving and charging modes are achieved. Excitation and demagnetization processes are accelerated in both generator control unit (GCU) driving mode and pure battery driving mode due to the multilevel voltage, which increase the torque capability. The battery can be directly charged by utilizing the traction motor windings and converter circuit, achieving a more compact and integrated converter topology. Micro-current charging is achieved by demagnetization currents in GCU or PV driving conditions. During the braking process, the energy can be flexibly recycled to the battery. In SHEB standstill conditions, the battery can be quickly charged by the PV panels and GCU/AC grids, which reduces the reliance on charging stations.

## II. Conventional SRM Drives

A conventional three-phase 12/8 SRM drive is shown in Fig. 1, including the SRM, power converter, drive circuit, position detection, and current detection. The phase currents are detected by current sensors for current control to generate drive signals for the power converter. An asymmetrical half-bridge converter is usually adopted in SRM drives, due to its phase isolation characteristic and excellent fault-tolerant ability. Each bridge arm is controlled independently by two switches.

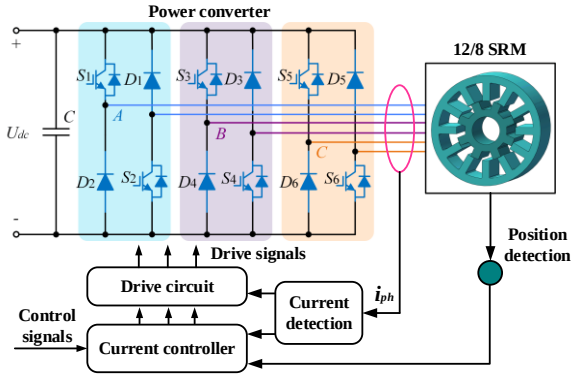


Fig. 1. Diagram of the three-phase 12/8 SRM drive.

The SRM can be modeled using electromagnetic equations [33], [34]. The models of the SRM are analyzed in details in [33], including the magnetic flux linkage and electromagnetic torque. Governing equations and physical modeling of a SRM are presented in [34] by assuming a linear magnetic circuit. Considering that the flux linkage of a phase is related to both the rotor position and phase current, the equation for each phase can be expressed as [33]-[36]

$$\begin{aligned} U_k &= R_k i_k + \frac{d\varphi_k}{dt} = R_k i_k + \frac{\partial \varphi_k}{\partial i_k}\frac{di_k}{dt} + \frac{\partial \varphi_k}{\partial \theta}\frac{d\theta}{dt} \\ &= R_k i_k + L_k(\theta, i_k)\frac{di_k}{dt} + \frac{\partial L_k(\theta, i_k)}{\partial \theta}\omega i_k \end{aligned} \tag{1}$$

where $U_k$ is the phase voltage, $R_k$ is the phase resistance, $\varphi_k$ is the flux, $i_k$ is the phase current, $\theta$ is the rotor position, $L_k$ is the phase inductance, $\omega$ is the angular speed, and $k$=$a$, $b$, $c$ phase. When a phase is turned on, positive dc-link voltage is applied to the phase winding and $U_k$=$U_{dc}$, where $U_{dc}$ is the dc-link voltage; when the upper switch is off and lower switch is on, $U_k$=0; when a phase is turned off, negative dc-link voltage is applied to the phase winding and $U_k$=-$U_{dc}$.

When a phase winding is energized by a positive dc-link voltage, it works in an excitation mode. In the demagnetization or braking mode, the phase is under a negative dc-link voltage.

The phase inductance varies as a function of the rotor position, and the output torque of the three-phase SRM is expressed as

$$T_e = \sum_{k=1}^{3} T_{ek} = \sum_{k=1}^{3} \frac{1}{2} i_k^{\,2} \frac{\partial L_k(i_k, \theta)}{d\theta} \tag{2}$$

The torque direction is forward when a current is applied to a phase winding in the phase inductance ascending region. Otherwise, a backward torque is produced in the phase inductance descending region.

The mechanical motion equation of the SRM is given by

$$J\frac{d\omega}{dt}+\mu\omega=T_e-T_l \tag{3}$$

where $T_e$ is the total electromagnetic torque, $T_l$ is the load torque, $J$ is the combined moment of inertia of the motor and load, and $\mu$ is the combined friction coefficient of the motor and load.

Fig. 2 illustrates the relationship of the phase inductance, phase current, phase voltage, and torque, where Region I is the motoring region and Region II is the braking region. As shown in Fig. 2(a), the positive or negative torque can be obtained by controlling the phase current flowing in the inductance ascending or descending region, respectively. Fig. 2(b) shows the motoring conditions under different excitation and demagnetization voltages. The current rises slowly when the excitation voltage is low, and a negative torque is easily generated due to the demagnetization current existing in the inductance descending region, which degrades the motoring performance. However, this negative torque can be eliminated by increasing the excitation and demagnetization voltage, and the output torque can be enhanced accordingly.

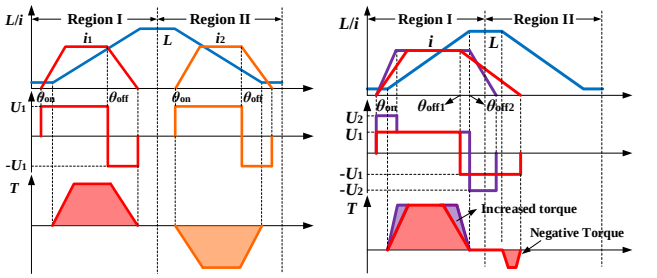


Fig. 2. Relationship of the phase inductance, phase voltage, and torque. (a) Motoring and regenerative braking modes. (b) Motoring under higher demagnetization voltages.

For a conventional SRM drive, multilevel voltage cannot be achieved due to a constant dc-link voltage, where the output torque is limited in high-speed operations. Also, multi-source operation and flexible charging functions are not equipped because only one source is connected to the converter circuit. This paper mainly focuses on developing a bidirectional multiport converter topology for SHEB applications. Compared to the conventional SRM drive, the presented topology has several advantages, including multi-source operation, improved torque performance, and flexible self-charging functions. PV panels are employed to extend the driving range and reduce the reliance on charging stations. The torque is improved due to the multi-source operation. The self-charging functions are directly achieved by using the motor windings and converter circuit. Multiple driving and charging modes are achieved by the proposed SRM drive, which will be analyzed in detail in the next section.

## III. Proposed Multiport Bidirectional SRM Drives for SHEB Application

### A. Proposed Multiport Bidirectional SRM Drive Topology

The diagram of the proposed SRM-based SHEB powertrain is schematically shown in Fig. 3. It consists of an energy storage unit, i.e., a battery bank, a power control unit including the multiport converter and controller, a GCU, an AC/DC converter for rectification, PV panels, and an SRM using as the traction motor. In this configuration, PV panels are introduced on the top of the bus to provide a sustainable power supply, which not only overcome the drawbacks of short driving range in pure battery working mode due to the limitation of current battery technologies, but also achieve flexible self-charging functions to reduce the reliance on charging stations.

Fig. 4 presents the proposed multiport bidirectional SRM drive topology for SHEB applications, which is composed of a bidirectional front-end circuit, a front-end PV-fed circuit, and a conventional asymmetrical half-bridge converter. The front-end circuits include a generator (G), a battery bank (B), PV panels (PV), a rectifier (RE), two capacitors ($C_1$ and $C_2$). Moreover, two insulated-gate bipolar transistors (IGBTs) ($S_{f1}$ and $S_{f2}$) integrated with fast recovery antiparallel diode, two diodes ($D_{f1}$ and $D_{f2}$), and three relays ($J$, $J_1$, and $J_2$) are employed to achieve multiple functions.

The demagnetization voltage is boosted to improve the torque by the battery bank in the GCU driving mode, where a trickle current charging is achieved; and by the capacitor $C_1$ in the battery driving mode. The GCU and battery bank can cooperate according to different working conditions, to improve the dynamic performance. The PV panels can be put into use as a sustainable energy source when the solar irradiance is sufficient, to reduce the reliance on fuels/batteries for increased driving range. Furthermore, flexible battery charging can be achieved when the bus is in standstill condition, where the battery bank can be charged by the PV source when the solar irradiance is sufficient and by the GCU/AC grids when the solar irradiance is insufficient, without external charging converters, which will significantly reduce the reliance on charging stations.

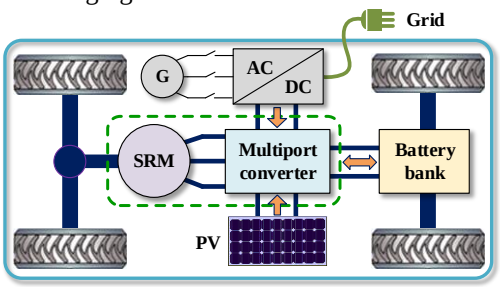


Fig. 3. Proposed SHEB propulsion system with self-charging functions.

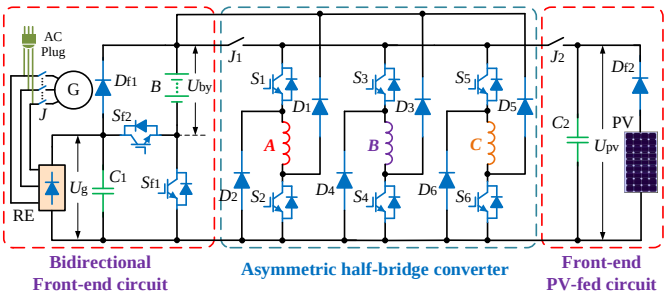


Fig. 4. Proposed multiport bidirectional SRM drive topology.

Fig. 5 shows the simplified system diagram of the proposed SRM drive for motoring and charging modes, respectively. The

This article has been accepted for publication in a future issue of this journal, but has not been fully edited. Content may change prior to final publication. Citation information: DOI 10.1109/TPEL.2017.2780622, IEEE Transactions on Power Electronics



GCU is mechanically coupled with an internal combustion engine (ICE) to provide three-phase AC power source for rectification. In motoring mode, the battery and GCU can work independently or cooperate by controlling the relay $J$ and switch $S_{f2}$ in the bidirectional circuit. The PV is selected for utilization by controlling the relay $J_2$ according to the solar irradiance. Thus, six driving modes are achieved, including GCU driving mode, battery driving mode, GCU and battery driving mode, PV and GCU driving mode, PV and battery driving mode, and PV driving mode, as shown in Fig. 5(a). In battery charging mode, by controlling the relays $J$ and $J_2$, three charging modes are achieved, including PV charging mode, GCU charging mode, and AC grids charging mode, as shown in Fig. 5(b).

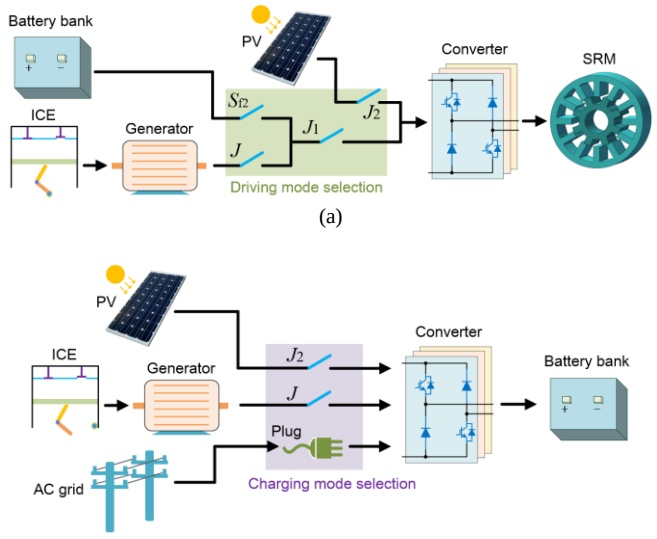


Fig. 5. Simplified system diagram of the proposed SRM drive. (a) Motoring mode. (b) Charging mode.

### B. Driving by the GCU and/or Battery Bank under Insufficient Solar Irradiance

When the solar irradiance is not sufficient, the GCU and/or battery bank are put into use, where the relay $J_1$ is on and $J_2$ is off, and the PV is in an idle state. The motor can be driven by the GCU and battery working together or independently, by controlling the power switches in the bidirectional front-end circuit. The winding excitation and demagnetization are both analyzed in GCU and/or battery driving mode in the following part.

*1) Winding Excitation Modes*:

Fig. 6 presents different winding excitation states for the proposed SRM drive. When the relay $J$ is on, and switches $S_{f1}$ and $S_{f2}$ are both off, the motor works in the GCU driving mode and the battery is in an idle state, as shown in Fig. 6(a). When $J$ is turned off, the GCU is idle and the windings are energized by the battery bank, where the motor works in the pure battery driving mode, as shown in Fig. 6(b). When the GCU and battery should be used together to improve the dynamic performance, $J$ and $S_{f2}$ are both turned on, where the windings are energized by both the GCU and battery bank, as shown in Fig. 6(c). A freewheeling mode when the current flows in a zero-voltage loop exists during the normal operation, due to the soft-chopping method where $S_1$ is turned off and $S_2$ remains on in the turn-on region, as illustrated in Fig. 6(d). The GCU and battery can work together or independently, according to different running conditions.

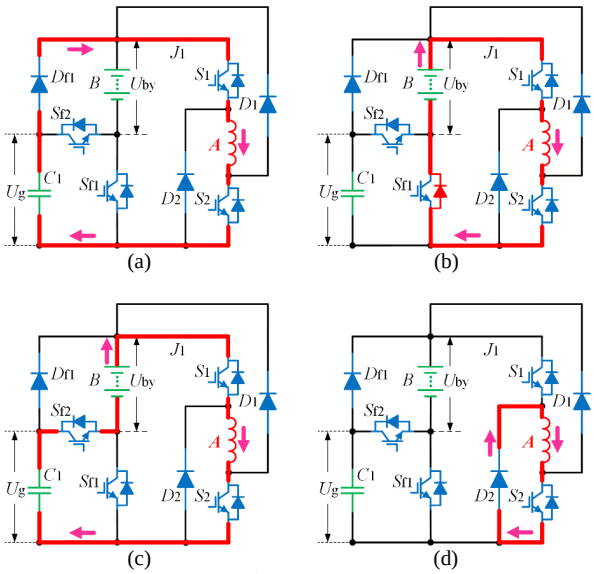


Fig. 6. Winding excitation states of the proposed SRM drive. (a) Excitation by the GCU. (b) Excitation by the battery bank. (c) Excitation by the GCU and battery bank. (d) Freewheeling in a zero-voltage loop.

*2) Winding Demagnetization Modes*:

In the GCU driving mode, the battery is idle when the GCU supplies the energy to the motor, where it can be used to boost the dc-link voltage to accelerate the demagnetization and excitation progresses. The relationship between the current and voltage of phase A during the commutation region is shown in Fig. 7(a), where a multilevel voltage is achieved.

Taking the commutation of phase A and B for example, when phase A is turned off and phase B is not turned on, the demagnetization current of phase A flows back to the battery bank $B$ and capacitor $C_1$ through the antiparallel diode inherent in the switch $S_{f2}$, where the battery is charged by the demagnetization current, as shown in Fig. 8(a). The phase A winding is under the demagnetization voltage of the battery bank $B$ and capacitor $C_1$. The voltage and current of phase A, i.e., $U_a$ and $i_a$, are expressed as

$$\begin{cases} U_a = -U_g - U_{by} = R_a i_a + L_a(\theta, i_a)\dfrac{di_a}{dt} + \dfrac{\partial L_a(\theta, i_a)}{\partial \theta}\omega i_a \\ i_a = i_{dc} \end{cases} \quad (4)$$

where $U_g$ is the capacitor voltage from the rectification of the GCU output, $U_{by}$ is the battery voltage, and $i_{dc}$ is the lower dc-link current.

When phase B is turned on and the demagnetization current $i_a$ is larger than the excitation current $i_b$, the phase A acts as a current source to power phase B. In this condition, phase A is still under the demagnetization voltage of the battery bank $B$ and capacitor $C_1$, and phase A current not only feeds back to the battery and capacitor, but also flows to phase B to help phase B set up the excitation current, as shown in Fig. 8(b). The voltage and current of phase A during this stage are given by

$$\begin{cases} U_a = -U_g - U_{by} = R_a i_a + L_a(\theta, i_a)\dfrac{di_a}{dt} + \dfrac{\partial L_a(\theta, i_a)}{\partial \theta}\omega i_a \\ i_a = i_{dc} + i_b \end{cases} \quad (5)$$

When the demagnetization current $i_a$ is smaller than the excitation current $i_b$, phase A current cannot support the excitation of phase B, and the GCU makes up for the energy deficit, as shown in Fig. 8(c). In this condition, phase A is under the demagnetization voltage of the capacitor $C_1$, and the voltage and current of phase A in this stage are expressed as

$$\begin{cases} U_a = -U_g = R_a i_a + L_a(\theta, i_a)\dfrac{di_a}{dt} + \dfrac{\partial L_a(\theta, i_a)}{\partial \theta}\omega i_a \\ i_a = -i_{dc} + i_b \end{cases} \quad (6)$$

When phase A is still in the demagnetization process and phase B current is in a zero-voltage loop (see Fig. 8(d)), there is no overlapped current loop between phase A and phase B. In this condition, phase A is again under the demagnetization voltage of the battery bank $B$ and capacitor $C_1$. The voltage and current of phase A during this stage can be expressed as (4).

Similar to the demagnetization process, the excitation voltage of phase A is also boosted, due to the impact of the phase C demagnetization, as shown in Fig. 7(a). When the demagnetization current $i_c$ is larger than the excitation current $i_a$, the phase C acts as a current source not only to power phase A, but also to charge the battery bank and capacitor. In this condition, phase A voltage is boosted due to the phase C demagnetization under the voltage of the battery bank $B$ and capacitor $C_1$. The voltage and current of phase A during this stage are given by

$$\begin{cases} U_a = U_g + U_{by} = R_a i_a + L_a(\theta, i_a)\dfrac{di_a}{dt} + \dfrac{\partial L_a(\theta, i_a)}{\partial \theta}\omega i_a \\ i_a = -i_{dc} + i_c \end{cases} \quad (7)$$

In the battery driving mode, the GCU is idle when the battery supplies energy to the motor, where the capacitor $C_1$ is used to elevate the dc-link voltage to accelerate the demagnetization and excitation processes. The working modes are similar to the GCU driving mode, and the only difference is that the battery bank acts as a power source instead of the GCU, and the capacitor $C_1$ is recharged as an additional source for multilevel production during the commutation regions, as shown in Fig. 7(b).

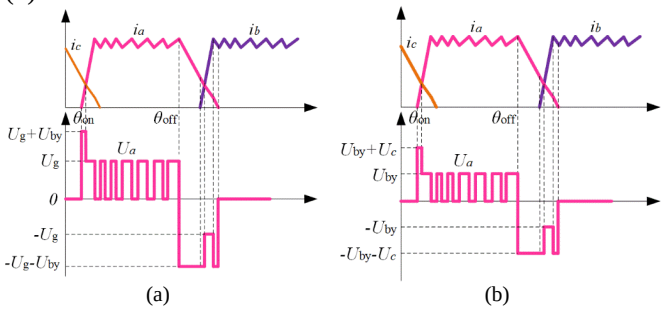


Fig. 7. Improved phase current and voltage in commutation region. (a) Driving by the GCU. (b) Driving by the battery bank.

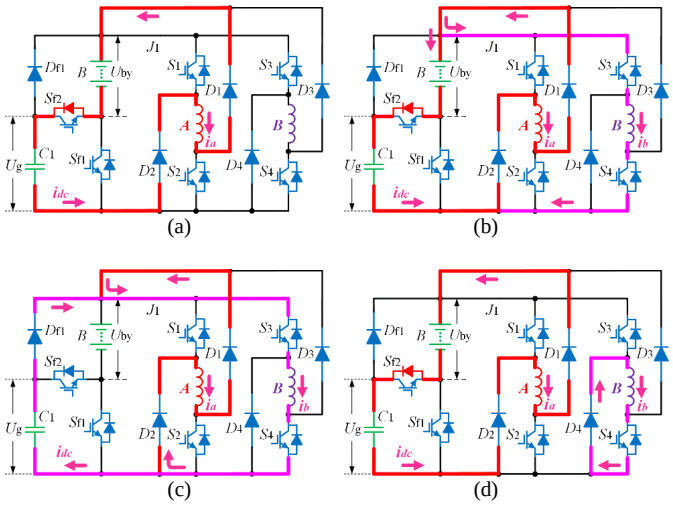


Fig. 8. Winding demagnetization states of the proposed SRM drive. (a) Stage 1. (b) Stage 2. (c) Stage 3. (d) Stage 4.

### *C. Driving by Hybrid Power Source with PV Auxiliary under Sufficient Solar Irradiance*

When the solar irradiance is sufficient, the PV is put into use as an assisted sustainable energy source to contribute to the motor driving, which reduces the reliance on fuels/batteries. In this case, the relays $J_1$ and $J_2$ are both turned on to connect the PV and GCU/battery to the main converter.

In the PV and GCU driving mode, switches $S_{f1}$ and $S_{f2}$ are both turned off, where $S_{f1}$ acts as a diode that is cutoff due to the lower voltage compared to the $C_1$ voltage. Thus, the battery is disconnected from the circuit. In this condition, the PV is paralleled with the GCU, and the equivalent power source circuit is shown in Fig. 9(a). The PV voltage is clamped to the GCU voltage $U_g$, and the working point of the PV is presented in Fig. 9(c). The PV and GCU work together to supply the energy to the motor drive. Each phase encounters three working states including the winding excitation, winding demagnetization, and freewheeling states, as shown in Fig. 10.

In the PV and battery driving mode, the GCU is disconnected from the circuit by turning off the relay $J$, and $S_{f1}$ is turned on. The PV is paralleled with the battery bank, and the equivalent power source circuit is shown in Fig. 9(b). The PV voltage is clamped to the battery voltage $U_{by}$, and the working point of the PV is presented in Fig. 9(d). The PV and battery work together to supply the energy to the motor drive, and the working modes for one phase are illustrated in Fig. 11, where the only difference from the PV-GCU driving mode are that the GCU is changed to the battery bank.

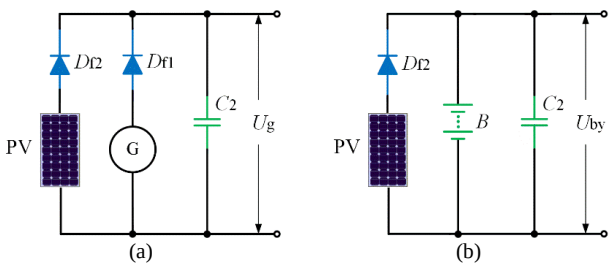

This article has been accepted for publication in a future issue of this journal, but has not been fully edited. Content may change prior to final publication. Citation information: DOI 10.1109/TPEL.2017.2780622, IEEE Transactions on Power Electronics



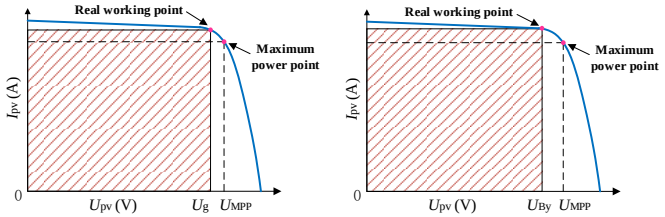


Fig. 9. Equivalent circuit of hybrid power source with PV auxiliary. (a) PV and GCU driving. (b) PV and battery driving. (c) Working point of the PV with GCU driving. (d) Working point of the PV with battery driving.

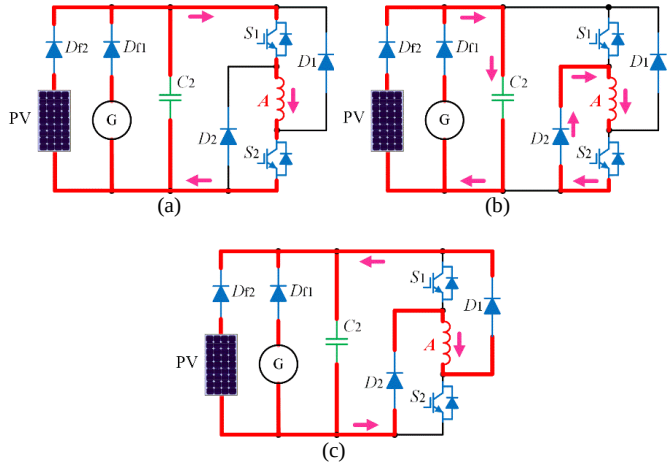


Fig. 10. Working modes in PV and GCU driving condition. (a) Winding excitation mode. (b) Freewheeling mode. (c) Winding demagnetization mode.

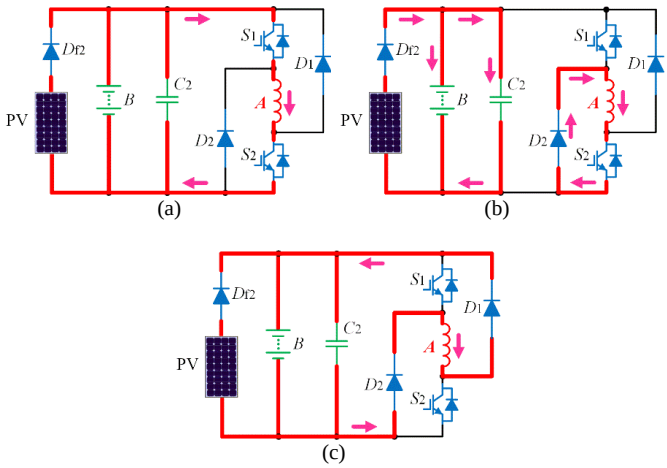


Fig. 11. Working modes in PV and battery driving condition. (a) Winding excitation mode. (b) Freewheeling mode. (c) Winding demagnetization mode.

### D. Driving by PV Panels in Downhill Motoring Condition

Given the low power density of the PV panels, they are insufficient to drive the motor under normal driving conditions. However, in downhill motoring condition, there is only limited energy required to power the motor. The energy generated from the PV source would be more than the SRM needed. Therefore, the PV source under this motoring condition could be sufficient to drive the motor. In this condition, relays $J$ and $J_1$ are turned off, $J_2$ is turned on, and the switch $S_{f1}$ is turned on and $S_{f2}$ is off. The equivalent circuit is presented in Fig. 12. The winding excitation, winding demagnetization, and freewheeling states are shown in Fig. 13. The PV panels supply the energy independently to the motor in the winding excitation mode, and in the winding demagnetization mode, the battery charging is achieved by the demagnetization current.

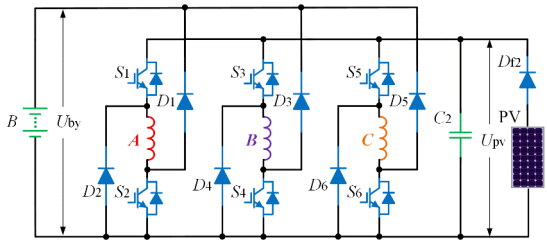


Fig. 12. Equivalent circuit in PV driving condition.

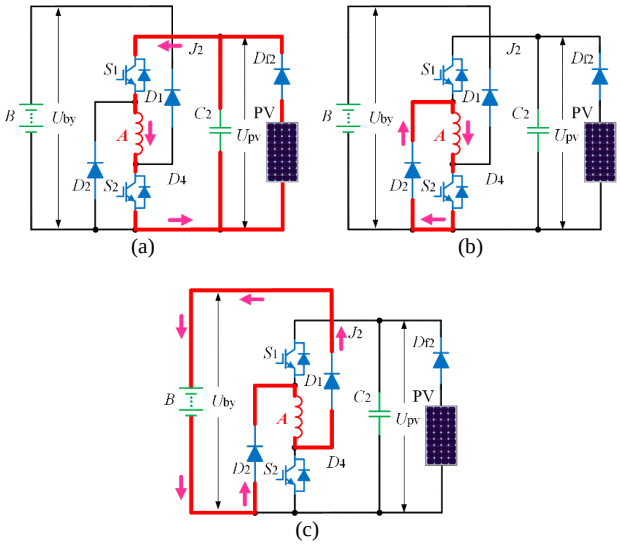


Fig. 13. Working modes in PV driving condition. (a) Winding excitation mode. (b) Freewheeling mode. (c) Winding demagnetization mode.

### E. Battery Charging Modes under SHEB Standstill Condition

#### 1) PV Powered Battery Charging

The proposed converter topology has integrated with on-board self-charging functions, which significantly reduces the reliance on charging stations. In SHEB standstill condition, the battery bank can be directly charged through the multiport SRM drive, without external charging converters. The self-charging can be achieved by the PV or GCU, and the external charging can be achieved by the AC grids.

When the solar irradiance is sufficient, the battery bank can be charged by the PV source. Due to the low power level of PV panels, only one phase converter is employed in the PV powered charging state. In this condition, the relay $J_1$ is off and $J_2$ is on, and the switches $S_{f1}$ is on and $S_{f2}$ is off. The phase windings are employed as inductors, and the driving topology functions as a buck-boost charging converter. The working modes are similar to the PV driving condition. PWM control signals can be applied to the power switches to achieve battery charging. Taking phase B for example, the PV source supplies the energy to the phase B winding, when $S_3$ and $S_4$ are both turned on simultaneously, as shown in Fig. 14(a). In this working state, the current flowing in the winding can be expressed as

$$i_{k1}(t) = I_{k0} + \frac{I_{km} - I_{k0}}{DT} t \tag{8}$$

This article has been accepted for publication in a future issue of this journal, but has not been fully edited. Content may change prior to final publication. Citation information: DOI 10.1109/TPEL.2017.2780622, IEEE Transactions on Power Electronics



where $I_{k0}$ is the initial phase current, $I_{km}$ is the maximum phase current, $T$ is the switching period, and $D$ is the duty cycle of the switching PWM, respectively.

Then, turning off the switches $S_3$ and $S_4$, the current in the phase winding feeds back to the battery bank $B$ through diodes $D_3$ and $D_4$, as shown in Fig. 14(b). In this working state, battery charging by the PV panels is achieved, and the charging current can be expressed as

$$i_{k2}(t) = I_{km} - \frac{I_{km} - I_{k0}}{(1-D)T}(t - DT) \tag{9}$$

By controlling the duty cycle and frequency of the PWM signals, the charging current can be easily controlled.

*2) GCU/AC grids Powered Battery Charging*

When the solar irradiance is insufficient, the battery bank can also be charged by the GCU/AC grids, where the working states are similar to the condition of PV charging. The only difference is that three phase windings are all included due to the high power level. In this state, the relay $J_1$ is on and $J_2$ is off, and the switches $S_{f1}$ and $S_{f2}$ are both off. Three phase windings are first energized by the energy from the capacitor $C_1$ when $S_1$~$S_6$ are all turned on, as shown in Fig. 14(c). Then, turning off switches $S_1$~$S_6$, the currents in the three phase windings goes back to the battery bank $B$ and capacitor $C_1$ through diodes $D_1$~$D_6$, as shown in Fig. 14(d). From Fig. 14(c) to (d), the battery bank can be flexibly charged by the DC output from the rectification of the GCU/AC grids, through controlling the duty cycle and frequency of the PWM signals.

Therefore, considering that three phase windings are all used, the maximum and minimum sum of three phase currents are

$$\begin{cases} I_{\max} = I_{am} + I_{bm} + I_{cm} \\ I_{\min} = I_{a0} + I_{b0} + I_{c0} \end{cases} \tag{10}$$

The charging current for the battery bank in this condition can be expressed as

$$i_{by}(t) = I_{\max} - \frac{I_{\max} - I_{\min}}{(1-D)T}(t - DT) \tag{11}$$

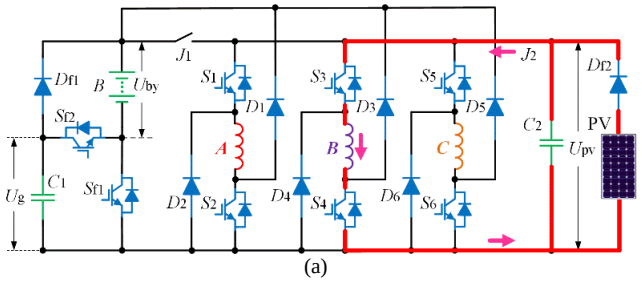


(a)

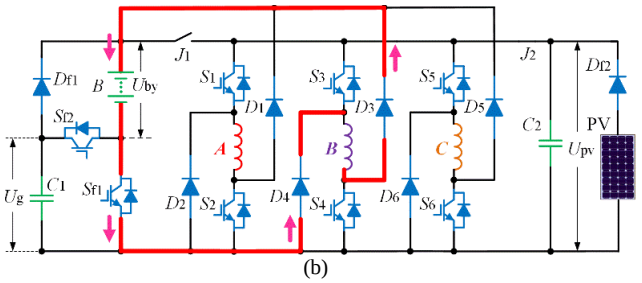


(b)

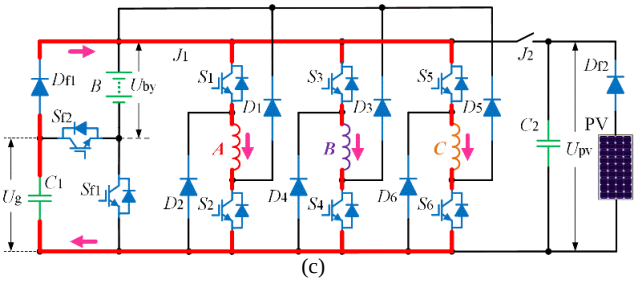


(c)

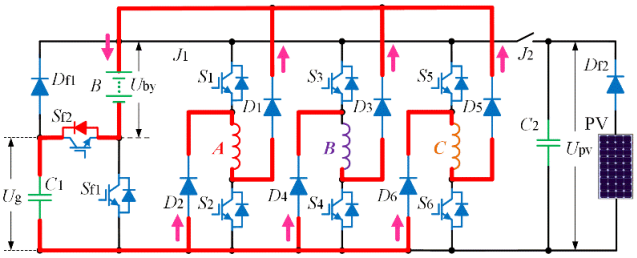


(d)

Fig. 14. Working modes under battery charging. (a) Winding excitation by the PV. (b) Battery charging from the PV. (c) Winding excitation by the rectification from the GCU/AC grids. (d) Battery charging by the rectification from the GCU/AC grids.

### *F. Power Control under Different Working Conditions*

Fig. 15 presents the power source cooperation among the GCU, battery bank, and PV at insufficient and sufficient solar irradiance conditions, respectively.

Fig. 15(a) shows the hybrid power source cooperation at different speeds when the solar irradiance is insufficient, where the PV is idle. During the SHEB starting and acceleration progresses, the GCU and battery can work together to increase the output torque to improve the start-up and acceleration performance, and the power flow is illustrated in Fig. 16(c). At low and high speeds, the GCU and battery can work independently for steady-state operations, where the output torque is improved by the boosted dc voltage, and the power flows are shown in Fig. 16(a) and (b). The energy can be recycled to the battery bank during braking conditions, by controlling the phase current flowing in the inductance descending region, as shown in Fig. 16(g). In SHEB standstill condition, the battery bank can be charged by the GCU/AC grids without external converters, and the power flows are presented in Fig. 16(h) and (j).

When the solar irradiance is sufficient, the PV can be put into use as a sustainable energy source for multiple functions, as shown in Fig. 15(b). In both low- and high-speed driving operations, the use of PV reduces the reliance on fuels/batteries for extended driving range, as shown in Fig. 16(d) and (e). In downhill condition, the PV panels can also supply the energy independently for motoring operation, as shown in Fig. 16(f). Furthermore, the battery self-charging is achieved by the solar energy in SHEB standstill condition, as shown in Fig. 16(i).

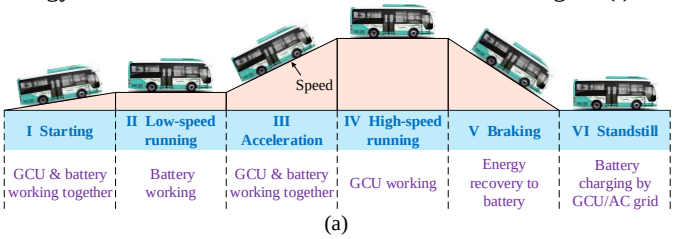


(a)

This article has been accepted for publication in a future issue of this journal, but has not been fully edited. Content may change prior to final publication. Citation information: DOI 10.1109/TPEL.2017.2780622, IEEE Transactions on Power Electronics



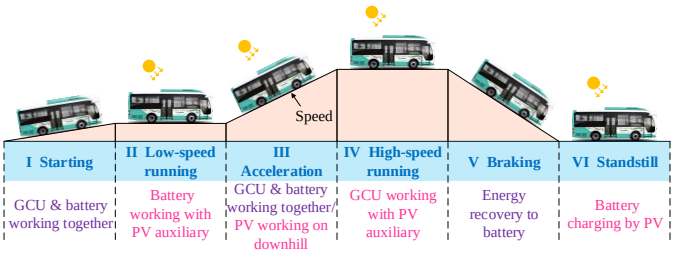


(b)

Fig. 15. Hybrid power source cooperation at different speeds. (a) Insufficient solar irradiance. (b) Sufficient solar irradiance.

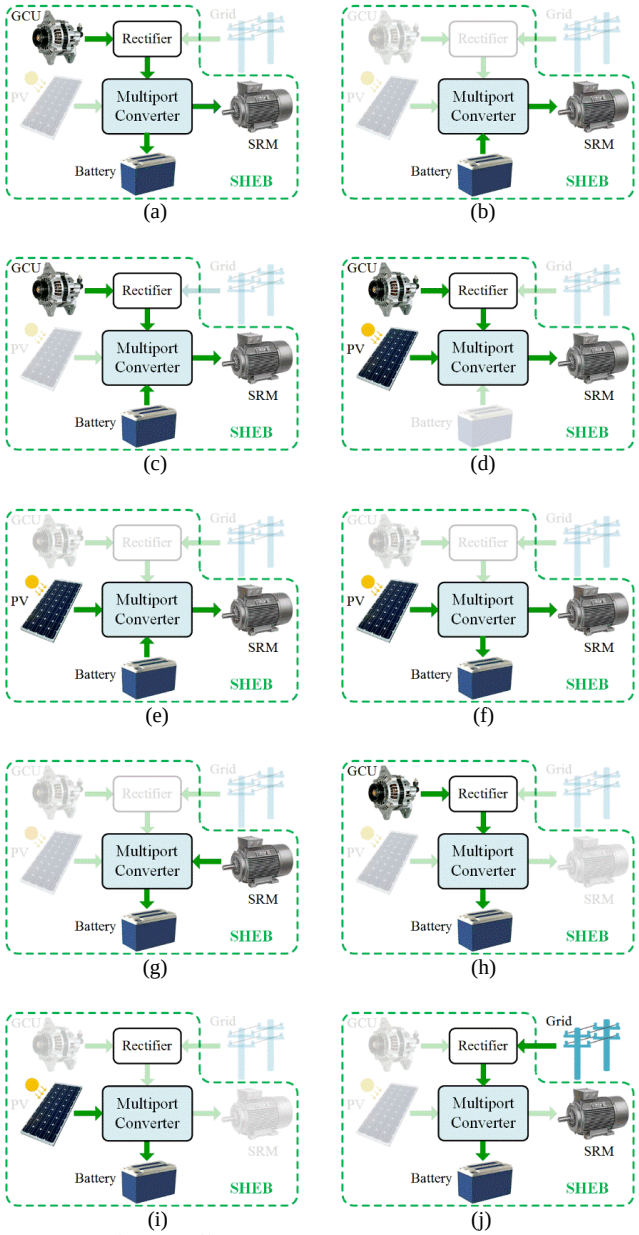


Fig. 16. Power flow at different working modes. (a) Motoring by the GCU. (b) Motoring by the battery. (c) Motoring by the GCU and battery. (d) Motoring by the GCU and PV. (e) Motoring by the battery and PV. (f) Downhill motoring by the PV. (g) Charging by the motor during braking process. (h) Self-charging by the GCU at standstill. (i) Self-charging by the PV at standstill. (j) Charging by AC grids at standstill.

### *G. Control Strategies for Motoring and Charging*

#### *1) Motoring Control Strategy*

The proposed SRM drive is derived from a traditional asymmetrical half-bridge converter, where the front-end circuit is used to achieve the multi-source operation. Fig. 17 presents the block diagram of the control strategy for motoring condition, where a conventional current hysteresis control method is employed for the motor drive. The hysteresis control system is a nonlinear system, which has excellent loop performance, global stability, and small phase lag [46]. The current hysteresis control is inherently stable and robust to dynamic perturbations, which is usually employed for SRM control. For current hysteresis control based SRM drives, the system is more stable and has fast dynamic response due to its inherent non-linearity [47], [48]. The dynamic analysis for SRM control has been investigated in detail in [33]-[36], [47]-[51]. The switching signals are derived from the comparison of the current reference and actual currents in the hysteresis controller. The rotor position is detected by an encoder for speed calculation, and the turn-on and turn-off angles are calculated for phase commutation. A proportional integral (PI) controller is employed to regulate the motor speed for closed-loop control, where the current reference is generated for hysteresis control. The motoring and braking operations are switched by controlling the turn-on and turn-off angles to make the current flow in the phase inductance ascending and descending regions, respectively. During the braking process, the battery bank is charged by the energy recovery.

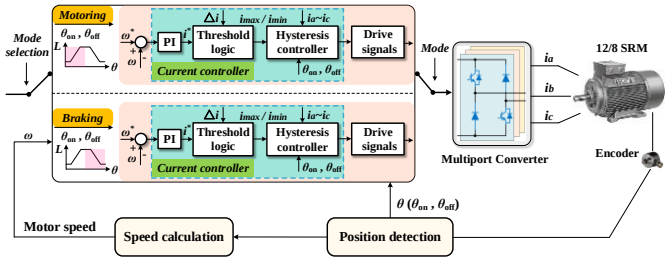


Fig. 17. Control block diagram for motoring conditions.

#### *2) Charging Control Strategy*

When the SHEB is in standstill condition, the battery bank can be charged by PV panels, ICE powered GCU or AC grids. Different control strategies are employed, according to the power level of the charging source, as shown in Fig. 18. Only one phase converter is employed in PV charging state, due to the low power level of PV panels. The corresponding control strategy is shown in Fig. 18 (a), where the MPPT stands for the maximum power point tracking. When the battery is charged by the GCU or AC grids, the power level is higher than the PV panels. For this scenario, the three-phase converter will work together to achieve high power charging. Due to the double saliency structure, the inductance of each phase is different from each other at a rotor position. In order to mitigate the influence of the unbalanced inductance, a current sharing control (CSC) method is proposed, and the corresponding control strategy is presented in Fig. 18(b).

This article has been accepted for publication in a future issue of this journal, but has not been fully edited. Content may change prior to final publication. Citation information: DOI 10.1109/TPEL.2017.2780622, IEEE Transactions on Power Electronics



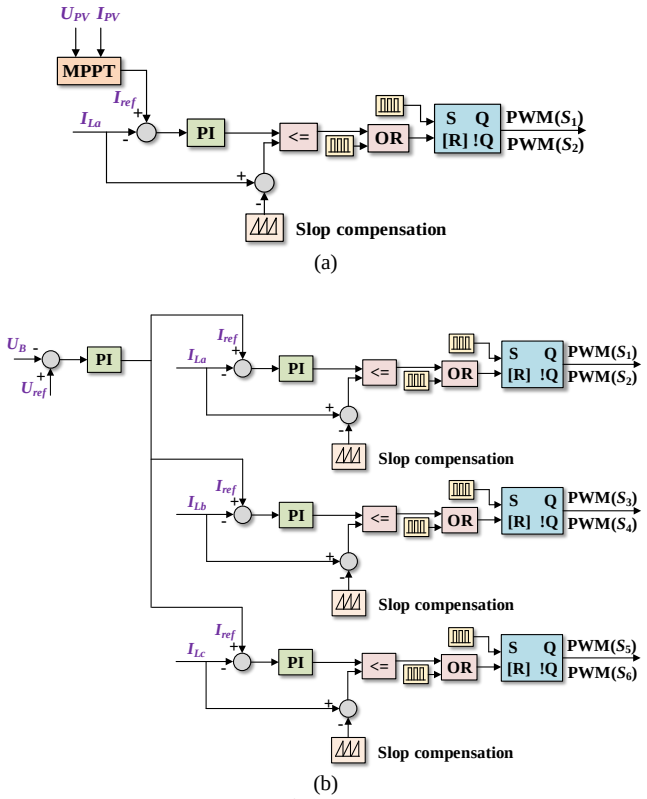


Fig. 18. Control block diagram for charging conditions. (a) PV powered charging. (b) Constant voltage control for GCU/AC grids charging.

There are two working modes for the boost converter, including the current discontinuous conduction mode (DCM) and current continuous conduction mode (CCM). In DCM, there is no right half-plane zero so that the converter is stable. In CCM, there is a right half-plane zero that impacts on the stability of the converter.

The charging transfer function from control to output voltage can be derived as

$$G_{vd1}(s)=\frac{D'(U_{by}+U_g)\left(\frac{L_a\cdot L_b+L_b\cdot L_c+L_c\cdot L_a}{L_a\cdot L_b\cdot L_c}-\frac{1}{RD'^2}s\right)}{Cs^2+\frac{1}{R}s+\frac{L_a\cdot L_b+L_b\cdot L_c+L_c\cdot L_a}{L_a\cdot L_b\cdot L_c}D'^2} \quad (12)$$

where $D$ is the duty cycle, $D'$=1-$D$, $C$ is the capacitor, $L_a$, $L_b$, $L_c$ are the phase winding inductances, and $R$ is the equivalent resistance.

The bode diagram of three-phase charging is plotted in Fig. 19(a), where the amplitude margin and phase margin are negative. From the transfer function and bode diagram, it can be seen that the system is a non-minimum phase system. In order to improve the system stability, the proportional integral (PI) compensation is adopted, and the corresponding transfer function is

$$G_{PI}(s)=k_p+\frac{k_i}{s} \quad (13)$$

The zero frequency of the PI regulator should be lower than the polar frequency of the transfer function of the standstill charging system. Based on this, the zero frequency of the PI regulator can be determined. After the calculation of the zero frequency, the proportional coefficient can adjust the cut-off frequency and stability margin. After the compensation, the improved bode diagram is shown in Fig. 19(b). From the amplitude margin and phase margin, it can be seen that the system is stable in this condition.

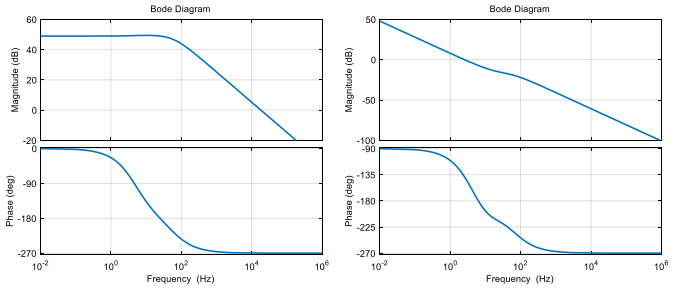


Fig. 19. Bode diagram under standstill charging conditions. (a) Without compensation. (b) With compensation.

### *H. Comparison with the State-of-the-Art Topologies*

A detailed comparison of the proposed SRM drive topology with existing schemes for electrified transportation is presented in Table I, which illustrates the advantages of the proposed drive topology over the state-of-the-art technologies. In [34]-[36], a dc-dc converter is employed for dc voltage boost and battery charging in pure battery-powered vehicle applications. However, additional inductors and capacitors reduce the power density, and also it has a high reliance on charging stations. An improved C-dump converter is presented in [37] for hybrid vehicles, while the boosted dc voltage cannot be achieved and the fault-tolerance ability is also poor due to the characteristics of the C-dump converter. To improve the fault-tolerance ability and charging ability, a split converter topology is developed in [38] with flexible energy control, while additional charging converters are required and the dc voltage cannot be boosted during running conditions. In [40], an integrated SRM converter is proposed for hybrid vehicles, where the dc voltage is enhanced and flexible battery charging is achieved. However, multiple ports are not achieved and flexible driving and self-charging ability are not equipped, which leads to a high reliance on batteries/fuels during driving conditions, and requires a high reliance on charging stations. Therefore, to extend the driving miles and reduce the reliance on charging stations, PV panels are employed in [45], but the developed converter is still derived from a C-dump converter, which has a poor fault-tolerance ability. Also, the dc voltage cannot be boosted to improve the torque capability.

Compared to existing drive topologies, PV panels are employed and multiport is achieved in the proposed motor drive, by using fewer power devices without extra dc-dc converters and inductors. The new topology is derived from an asymmetrical half-bridge converter, and thus has a good fault-tolerance ability. The dc voltage is boosted in both GCU and battery driving modes, where the torque capability is improved accordingly. Six driving modes and five charging modes are obtained, achieving a more flexible energy control. The PV can work with the battery/GCU together as an assisted sustainable energy source to contribute to the motor driving, which significantly reduces the reliance on fuels/batteries. Furthermore, the battery can be quickly charged by the PV panels, GCU, or AC grids at SHEB standstill condition, where the flexible charging and self-charging ability are obtained, and the reliance on charging stations is significantly reduced.

TABLE I
COMPARISON OF PROPOSED AND STATE-OF-THE-ART TOPOLOGIES

| | Drive topology in [34] | Drive topology in [35][36] | Drive topology in [37] | Drive topology in [38] | Drive topology in [40] | Drive topology in [45] | Proposed drive topology |
|---|---|---|---|---|---|---|---|
| Energy flow flexibility | Low | Medium | Low | Medium | Medium | Medium | High |
| Fault-tolerance ability | Yes | No | No | Yes | Yes | No | Yes |
| Grid connecting charging | Without charging converter | Without charging converter | Without charging converter | Need charging converter | Without charging converter | Need charging converter | Without charging converter |
| Multiport | Not achieved | Not achieved | Not achieved | Not achieved | Achieved | Not achieved | Achieved |
| Enhanced dc voltage | Yes | Yes | No | No | Yes | No | Yes |
| Self-charging ability | Not equipped | Not equipped | Not equipped | Not equipped | Not equipped | Equipped | Equipped |
| Reliance on batteries/fuels | High | High | High | High | High | Low | Low |
| Reliance on charging stations | High | High | High | High | High | Low | Low |

## IV. EXPERIMENTAL VERIFICATION

In order to verify the effectiveness of the proposed multiport SRM drive topology, the experiments are carried out on a three-phase 12/8 SRM prototype for proof-of-concept. The photograph of the experimental system is shown in Fig. 20, including the power electronics for the drive and motor test bed. The main motor parameters are listed in Table II. A dSPACE-DS1006 platform is employed to implement the control algorithm for the proposed system. In the motor test bed, a Parker AC servomotor acts as the load, which is controlled by an integrated load controller inside the cabinet. A high-precision torque sensor is installed between the SRM prototype and load motor to detect the instantaneous output torque. A three degree of freedom (3-DOF) bracket is used to achieve the balanced connection. A 2500-line incremental encoder is installed on the motor frame to detect the rotor position and calculate the motor speed. A programmable dc power supply is utilized to simulate the GCU part, where the voltage is set to 80 V. A 60 V lithium-ion battery pack is employed to be the energy storage equipment. A PV array simulator Agilent Technology E4360A is employed as the PV source. Hall-effect current sensors LA-55P are used to detect the phase currents for current regulation control. A multi-channel isolated oscilloscope is used to observe the experimental waveforms. A closed-loop controller with current hysteresis modulation is designed to control the phase currents for speed regulation.

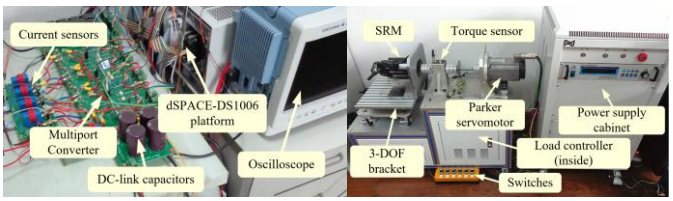


Fig. 20. Experimental setup.

TABLE II
MOTOR PARAMETERS

| Parameters | Value |
|---|---|
| Phase number | 3 |
| Stator/rotor poles | 12/8 |
| Rated power (W) | 750 |
| Rated speed (r/min) | 1500 |
| Phase resistor (Ω) | 3.01 |
| Minimum phase inductance (mH) | 27.2 |
| Maximum phase inductance (mH) | 256.7 |
| Rotor outer diameter (mm) | 55 |
| Rotor inner diameter (mm) | 30 |
| Stator outer diameter (mm) | 102.5 |
| Stator inner diameter (mm) | 55.5 |
| Stack length (mm) | 80 |
| Stator arc angle (deg) | 14 |
| Rotor arc angle (deg) | 16 |

Fig. 21 presents the experimental waveforms of the proposed motor drive operating at 280 r/min and 2 N·m load with only GCU or battery driving, where $i_a$, $i_b$, and $i_c$ are the phase currents for phase A, B, and C, respectively, $U_a$ is voltage of phase A winding, and $i_{by}$ is the battery current. In GCU driving mode, the generator supplies the energy to the motor drive, and the battery bank is idle. The multilevel phase voltage is directly achieved by the battery bank in the converter circuit although there is no power supply from the battery, where the excitation voltage and demagnetization voltage are both boosted to accelerate the winding excitation and demagnetization processes in the phase commutation region. Meanwhile, trickle current charging is achieved by the demagnetization current due to the inherent characteristics of the proposed drive, as shown in Fig. 21(a). Similarly, in pure battery driving mode, the generator is idle, and the battery acts as the power source to supply the energy to the motor drive. In this condition, the multilevel voltage can also be achieved by the capacitor $C_1$ in the circuit, where the operation modes are similar to that in Fig. 21(a), and the excitation and demagnetization processes are both accelerated due to the increased phase voltage, as shown in Fig. 21(b). Fig. 22(a) and (b) present the experimental results when the motor drive operates in GCU driving mode at 1800 r/min and GCU-battery driving mode at 2400 r/min, respectively. In high-speed operation, the phase voltage can also be boosted in the phase commutation region in GCU

This article has been accepted for publication in a future issue of this journal, but has not been fully edited. Content may change prior to final publication. Citation information: DOI 10.1109/TPEL.2017.2780622, IEEE Transactions on Power Electronics



driving mode, where the fast excitation and fast demagnetization are also both achieved, as shown in Fig. 22(a). Therefore, the torque output is improved accordingly due to the multilevel voltage, no matter in low- or high-speed operations.

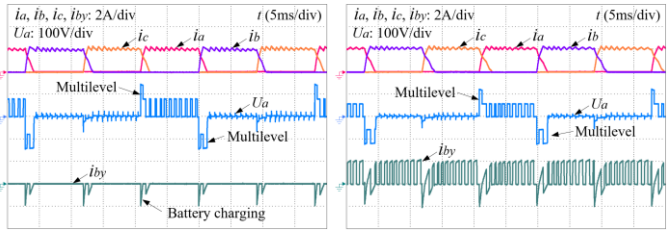


Fig. 21. Low-speed operation without PV auxiliary. (a) GCU Driving mode. (b) Battery driving mode.

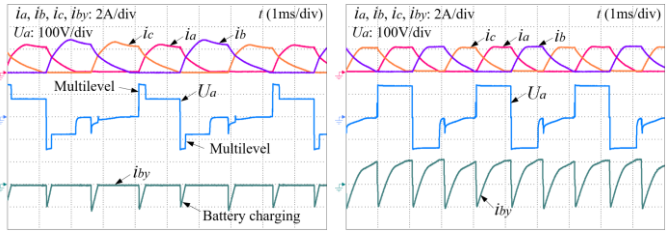


Fig. 22. High-speed operation without PV auxiliary. (a) GCU Driving mode. (b) GCU and battery driving mode.

The experimental waveforms of the proposed motor system driving by the hybrid power source with PV auxiliary at 400 r/min are shown in Fig. 23. In PV-GCU driving mode, the battery bank is disconnected from the converter circuit, and the PV source is paralleled with the GCU part to supply the power to the motor drive. According to the equivalent power source circuit, the PV voltage is clamped to the GCU voltage in this condition. Fig. 23(a) shows the experimental results in PV-GCU driving mode. The PV and GCU work together to supply the energy to the motor drive, which reduces the reliance on fuels. In PV-battery driving mode, the generator is disconnected from the converter circuit, and the PV source works with the battery to supply the power to the motor drive. Fig. 23(b) shows the experimental results in PV-battery driving mode. The PV is put into use as an assisted sustainable energy source to contribute to the motor driving, which reduces the reliance on batteries. Fig. 24 presents the waveforms under PV independent driving condition. The PV source supplies the energy to the motor drive and the battery bank can be charged by the demagnetization current, which is similar to that in GCU driving mode.

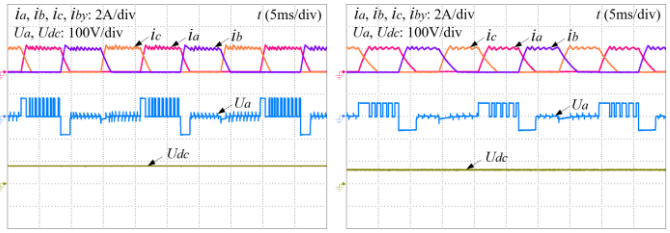


Fig. 23. Driving by the hybrid power source with PV auxiliary. (a) PV and GCU driving. (b) PV and battery driving.

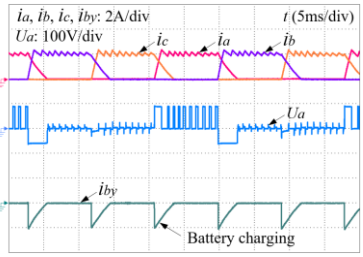


Fig. 24. Driving by the PV source under downhill motoring condition.

In order to investigate the dynamic performance of the proposed motor drive topology, Fig. 25 illustrates the transient progress during the speed change, load change, and braking conditions in a closed-loop system. In Fig. 25(a), the motor drive works in pure battery driving mode at 300 and 850 r/min, and in GCU driving mode at 1300 r/min in steady-state operations, while works in battery-GCU driving mode during acceleration process. The battery and generator can work together to improve the acceleration performance of the motor. When the speed reference increases from 300 to 850 r/min and from 850 to 1300 r/min, the actual speed quickly tracks the speed reference. During acceleration, the speed is stabilized within 1 s and follows the given value well, which ensures a fast response to speed changes. As shown in Fig. 25(b), when the load changes from 2 to 4 N·m, the speed is quickly stabilized and tracks the given value. Therefore, the proposed motor drive presents a rapid dynamic response to speed and load changes, confirming a good robustness. Fig. 25(c) and (d) show the experimental results of the braking performance for the proposed dive. The braking response time can be flexibly controlled by adjusting the turn-on and turn-off angles. In Fig. 25(c), the braking time is near 2 s when the turn-on angle and turn-off angles are set to 20° and 30°, respectively. In Fig. 25(d), the turn-off angle is increased to 40° and the braking time is only 0.7 s, ensuring a flexible braking ability. Moreover, during the braking process, the energy can be recycled to the battery bank directly through the proposed drive topology, as shown in Fig. 25(c) and (d).

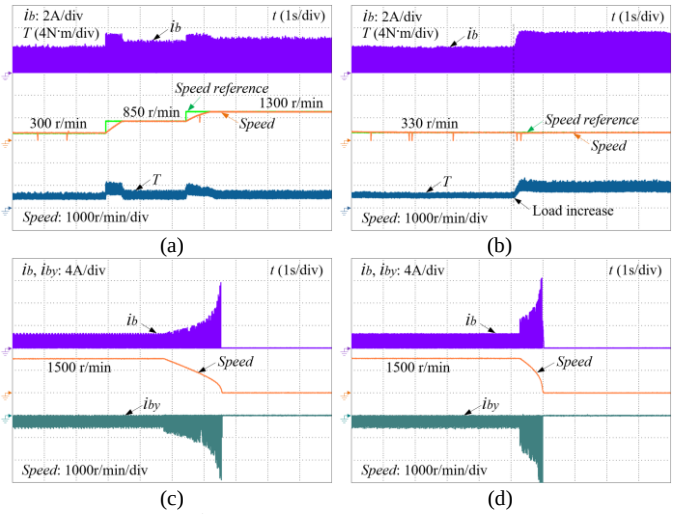


Fig. 25. Dynamic performance. (a) Speed increase. (b) Load increase. (c) Braking under turn-on angle 20° and turn-off angle 30°. (d) Braking under turn-on angle 20° and turn-off angle 40°.

The waveforms of battery charging by PV and AC grids in motor standstill conditions are shown in Fig. 26, where $P_z$ is the encoder signal, and $S_3$ and $S_4$ are the driving signals for phase B. The battery can be directly charged by utilizing the traction motor windings and converter drive, without any additional converters and inductors. The PWM signals are applied to the corresponding switches to control the battery charging current. When the battery is charged by the PV, one phase converter is employed due to the low power level. Fig. 26(a) and (b) show the battery charging by the PV using phase B leg and winding, where the switching frequency is set to 500 Hz and the duty cycle is set to 0.5 and 0.7, respectively. Switches $S_3$ and $S_4$ are both turned on first to energize the phase B winding, and then turned off simultaneously to make the phase current feed back to the battery bank through diodes $D_3$ and $D_4$. In this condition, battery charging by the PV is achieved, and the charging current can be flexibly controlled by changing the PWM frequency and duty cycle. When the battery is charged by AC grids, three phase windings are all employed due to the high power level, as shown in Fig. 26(c) and (d). Similarly, three phase windings work in excitation mode by turning on switches $S_1$~$S_6$, and then work in demagnetization mode by turning off all the switches, to achieve three-phase charging. The encoder signal keeps at zero, and thus the charging scheme does not lead to motor movement. Fig. 26(c) shows the charging condition without CSC scheme, where the three phase currents are unbalanced due to the different phase inductances. Therefore, to reduce the impact of the unbalanced inductance, the proposed CSC is adopted to balance the phase currents, as shown in Fig. 26(d).

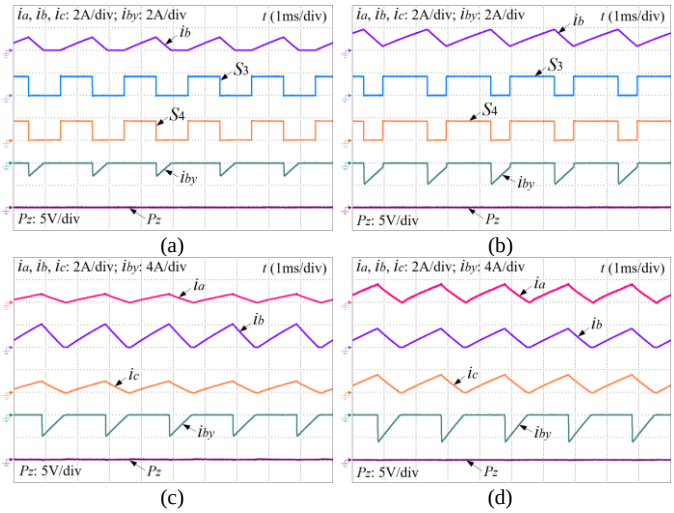


Fig. 26. Battery charging at SRM standstill states. (a) Charging by PV under duty-cycle 0.5. (b) Charging by PV under duty-cycle 0.7. (c) Charging by AC grids without CSC. (d) Charging by AC grids with CSC.

In order to investigate the torque performance of the proposed SRM drive, Figs. 27 and 28 present the torque and torque ripple comparisons between the traditional system by employing the conventional asymmetric half-bridge converter and the new system by employing the proposed multiport converter. As shown in Fig. 27, the torque is improved by fast winding excitation and fast winding demagnetization in both GCU and battery driving modes, especially in high-speed operations, due to the multilevel voltage generated in the phase commutation region. Regarding the torque ripple, the torque ripple between the conventional and proposed drives are similar, confirming that the proposed drive will not decrease the motor performance, as shown in Fig. 28.

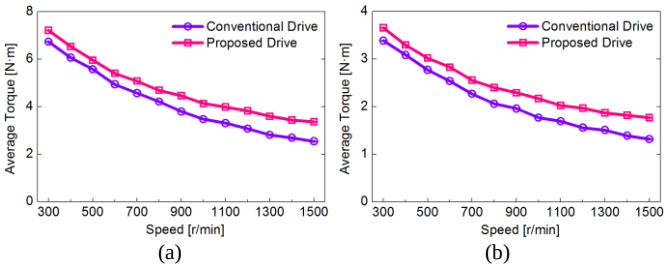


Fig. 27. Torque comparison. (a) GCU driving mode. (b) Battery driving mode.

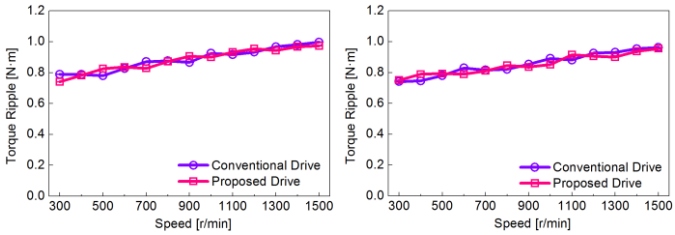


Fig. 28. Torque ripple comparison. (a) GCU driving mode. (b) Battery driving mode.

## V. Conclusion

In this paper, a multiport bidirectional SRM drive is proposed for SHEB applications, which not only improves the motor system performance in running conditions, but also achieves flexible charging functions. Multiple driving and charging modes are achieved. Multilevel voltage is obtained to increase the torque capability. PV panels are installed on the bus to extend the driving range and achieve self-charging ability. Corresponding working modes and control strategies are investigated in detail. The main contributions of this paper are as follows:

(1) A simple multiport bidirectional SRM drive is designed to combine the GCU, battery bank, PV panels, and SRM for flexible driving and charging functions, by using fewer power devices. The charging functions can be directly achieved by the motor windings and converter circuit.

(2) Six driving modes are achieved. When the solar irradiance is not sufficient, the SHEB can work in GCU driving mode, pure battery driving mode, and GCU-battery driving mode, according to the running conditions. When the solar irradiance is sufficient, the PV can work with the battery/GCU together as an assisted sustainable energy source to contribute to the motor driving, which significantly reduces the reliance on fuels/batteries. In addition, in downhill motoring condition, the PV can provide the energy independently to drive the motor.

(3) Five charging modes are achieved without external charging converters. The battery bank can be slightly charged by the demagnetization current in GCU driving mode and PV driving mode. During the braking progress, the energy can be recycled to the battery. Furthermore, the battery bank can be quickly charged by the PV panels, GCU, or AC grids at SHEB

standstill condition, which reduces the reliance on charging stations. Corresponding control strategies are presented to achieve the flexible energy control.

(4) The dc voltage is boosted and multilevel voltage is achieved by the battery bank in GCU driving mode, and by the charge capacitor in pure battery driving mode. The excitation and demagnetization processes are both accelerated due to the boosted dc voltage. The torque capability can be increased by 35% due to the multiport topology without torque ripple increase.

Although the work has targeted electrified vehicle applications, the developed technology can be applied to other high-torque and high-speed applications, such as more-electric aircraft, traction drives, and electrical ships.

## REFERENCES


[1] A. A. Ferreira, J. A. Pomilio, G. Spiazzi, and L. de Araujo Silva, "Energy management fuzzy logic supervisory for electric vehicle power supplies system," *IEEE Trans. Power Electron.*, vol. 23, no. 1, pp. 107-115, Jan. 2008.

[2] G. Carli and S. S. Williamson, "Technical considerations on power conversion for electric and plug-in hybrid electric vehicle battery charging in photovoltaic installations," *IEEE Trans. Power Electron.*, vol. 28, no. 12, pp. 5784-5792, Dec. 2013.

[3] O. C. Onar, J. Kobayashi, and A. Khaligh, "A fully directional universal power electronic interface for EV, HEV, and PHEV applications," *IEEE Trans. Power Electron.*, vol. 28, no. 12, pp. 5489-5498, Dec. 2013.

[4] S. S. Williamson, A. K. Rathore, and F. Musavi, "Industrial electronics for electric transportation: current state-of-the-art and future challenges," *IEEE Trans. Ind. Electron.* vol. 62, no. 5, pp. 3021-3032, May 2015.

[5] A. Emadi, Y. J. Lee, and K. Rajashekara, "Power electronics and motor drives in electric, hybrid electric, and plug-in hybrid electric vehicles," *IEEE Trans. Ind. Electron.*, vol. 55, no. 6, pp. 2237–2245, Jun. 2008.

[6] Z. Yang, F. Shang, I. P. Brown, and M. Krishnamurthy, "Comparative study of interior permanent magnet, induction, and switched reluctance motor drives for EV and HEV applications," *IEEE Trans. Transport. Electrific.*, vol. 1, no. 3, pp. 245-254, Oct. 2015.

[7] F. Mwasilu and J. W. Jung, "Enhanced fault-tolerant control of interior PMSMs based on an adaptive EKF for EV traction applications," *IEEE Trans. Power Electron.*, vol. 31, no. 8, pp. 5746-5758, Aug. 2016.

[8] Y. Miyama, M. Hazeyama, S. Hanioka, N. Watanabe, A. Daikoku, and M. Inoue, "PWM carrier harmonic iron loss reduction technique of permanent-magnet motors for electric vehicles," *IEEE Trans. Ind. Appl.*, vol. 52, no. 4, pp. 2865-2871, Jul./Aug. 2016.

[9] A. Choudhury, P. Pillay and S. S. Williamson, "Modified dc-bus voltage-balancing algorithm based three-level neutral-point-clamped IPMSM drive for electric vehicle applications," *IEEE Trans. Ind. Electron.*, vol. 63, no. 2, pp. 761-772, Feb. 2016.

[10] N. Bianchi, S. Bolognani, E. Carraro, M. Castiello, and E. Fornasiero, "Electric vehicle traction based on synchronous reluctance motors," *IEEE Trans. Ind. Appl.*, vol. 52, no. 6, pp. 4762-4769, Nov./Dec. 2016.

[11] I. Boldea, L. N. Tutelea, L. Parsa, and D. Dorrell, "Automotive electric propulsion systems with reduced or no permanent magnets: an overview," *IEEE Trans. Ind. Electron.*, vol. 61, no. 10, pp. 5696-5711, Oct. 2014.

[12] S. Morimoto, O. Shohei, Y. Inoue, and M. Sanada, "Experimental evaluation of a rare-earth-free PMASynRM with ferrite magnets for automotive applications," *IEEE Trans. Ind. Electron.*, vol. 61, no. 10, pp. 5749-5756, Oct. 2014.

[13] M. Krishnamurthy, C. S. Edrington, A. Emadi, P. Asadi, M. Ehsani, and B. Fahimi, "Making the case for applications of switched reluctance motor technology in automotive products," *IEEE Trans. Power Electron.*, vol. 21, no. 3, pp. 659-675, May 2006.

[14] E. Bostanci, M. Moallem, A. Parsapour, and B. Fahimi, "Opportunities and challenges of switched reluctance motor drives for electric propulsion: a comparative study," *IEEE Trans. Transport. Electrific.*, vol. 3, no. 1, pp. 58-75, Mar. 2017.

[15] K. M. Rahman, B. Fahimi, G. Suresh, A. V. Rajarathnam, and M. Ehsani, "Advantages of switched reluctance motor applications to EV and HEV: design and control issues," *IEEE Trans. Ind. Appl.*, vol. 36, no. 1, pp. 111-121, Jan./Feb. 2000.

[16] A. Chiba, K. Kiyota, N. Hoshi, M. Takemoto, and S. Ogasawara, "Development of a rare-earth-free SR motor with high torque density for hybrid vehicles," *IEEE Trans. Energy Convers.*, vol. 30, no. 1, pp. 175-182, Mar. 2015.

[17] K. Kiyota, and A. Chiba, "Design of switched reluctance motor competitive to 60-kW IPMSM in third-generation hybrid electric vehicle," *IEEE Trans. Ind. Appl.*, vol. 48, no. 6, pp. 2303-2309, Nov./Dec. 2012.

[18] W. Hua, H. Hua, N. Dai, G. Zhao and M. Cheng, "Comparative study of switched reluctance machines with half-and full-teeth-wound windings," *IEEE Trans. Ind. Electron.*, vol. 63, no. 3, pp. 1414-1424, Mar. 2016.

[19] F. L. M. d. Santos, J. Anthonis, F. Naclerio, J. J. C. Gyselinck, H. V. d. Auweraer, and L. C. S. Góes, "Multiphysics NVH modeling: simulation of a switched reluctance motor for an electric vehicle," *IEEE Trans. Ind. Electron.*, vol. 61, no. 1, pp. 469-476, Jan. 2014.

[20] J. Ye, B. Bilgin, and A. Emadi, "An extended-speed low-ripple torque control of switched reluctance motor drives," *IEEE Trans. Power Electron.*, vol. 30, no. 3, pp. 1457-1470, Mar. 2015.

[21] B. Bilgin, A. Emadi, and M. Krishnamurthy, "Comprehensive evaluation of the dynamic performance of a 6/10 SRM for traction application in PHEVs," *IEEE Trans. Ind. Electron.*, vol. 60, no. 7, pp. 2564-2575, Jul. 2013.

[22] M. A. Kabir, and I. Husain, "Design of mutually coupled switched reluctance motors (MCSRMs) for extended speed applications using 3-phase standard inverters," *IEEE Trans. Energy Convers.*, vol. 31, no. 2, pp. 436-445, Jun. 2016.

[23] R. Martin, J. D. Widmer, B. C. Mecrow, M. Kimiabeigi, A. Mebarki, and N. L. Brown, "Electromagnetic considerations for a six-phase switched reluctance motor driven by a three-phase inverter," *IEEE Trans. Ind. Appl.*, vol. 52, no. 5, pp. 3783-3791, Sep./Oct. 2016.

[24] S. Song, Z. Xia, Z. Zhang, and W. Liu, "Control performance analysis and improvement of a modular power converter for three-phase SRM with Y-connected windings and neutral line," *IEEE Trans. Ind. Electron.*, vol. 63, no. 10, pp. 6020-6030, Oct. 2016.

[25] K. Tomczewski, and K. Wrobel, "Quasi-three-level converter for switched reluctance motor drives reducing current rising and falling times," *IET Power Electron.*, vol. 5, no. 7, pp. 1049-1057, Jul. 2012.

[26] A. Deriszadeh, E. Adib, H. Farzanehfard, and S. Mortaza Saghaeian Nejad, "Switched reluctance motor drive converter operating in continuous conduction mode with high demagnetisation voltage," *IET Power Electron.*, vol. 8, no. 7, pp. 1119-1127, Jul. 2015.

[27] M. A. Elgendy, V. Pickert, B. Zahawi, C. Morton, and A. Ayob, "Dual voltage supply converter for high-speed doubly salient reluctance motors," *IEEE Trans. Power Electron.*, vol. 28, no. 2, pp. 1016-1024, Feb. 2013.

[28] A. K. Jain, and N. Mohan, "SRM power converter for operation with high demagnetization voltage," *IEEE Trans. Ind. Appl.*, vol. 41, no. 5, pp. 1224-1231, Sep./Oct. 2005.

[29] D. H. Lee, and J. W. Ahn, "A novel four-level converter and instantaneous switching angle detector for high speed SRM drive," *IEEE Trans. Power Electron.*, vol. 22, no. 5, pp. 2034-2041, Sep. 2007.

[30] J. Liang, D. H. Lee, G. Xu, and J. W. Ahn, "Analysis of passive boost power converter for three-phase SR drive," *IEEE Trans. Ind. Electron.*, vol. 57, no. 9, pp. 2961-2971, Sep. 2010.

[31] T. Weng Kwai, and C. Pollock, "Low-cost battery-powered switched reluctance drives with integral battery-charging capability," *IEEE Trans. Ind. Appl.*, vol. 36, no. 6, pp. 1676-1681, Nov./Dec. 2000.

[32] M. Barnes, and C. Pollock, "Forward converters for dual voltage switched reluctance motor drives," *IEEE Trans. Power Electron.*, vol. 16, no. 1, pp. 83-91, Jan. 2001.

[33] F. Yi, and W. Cai, "A quasi-Z-source integrated multiport power converter as switched reluctance motor drives for capacitance reduction and wide-speed-range operation," *IEEE Trans. Power Electron.*, vol. 31, no. 11, pp. 7661-7676, Nov. 2016.

[34] H. C. Chang and C. M. Liaw, "On the front-end converter and its control for a battery powered switched-reluctance motor drive," *IEEE Trans. Power Electron.*, vol. 23, no. 4, pp. 2143-2156, Jul. 2008.

[35] H. C. Chang and C. M. Liaw, "An integrated driving/charging switched reluctance motor drive using three-phase power module," *IEEE Trans. Ind. Electron.*, vol. 58, no. 5, pp. 1763-1775, May 2011.

[36] K. Hu, P. Yi, and C. Liaw, "An EV SRM drive powered by battery/supercapacitor with G2V and V2H/V2G capabilities," *IEEE Trans. Ind. Electron.*, vol. 62, no. 8, pp. 4714-4727, Aug. 2015.

[37] Y. Hu, X. Song, W. Cao, and B. Ji, "New SR drive with integrated charging capacity for plug-in hybrid electric vehicles (PHEVs)," *IEEE Trans. Ind. Electron.*, vol. 61, no. 10, pp. 5722-5731, Oct. 2014.

[38] Y. Hu, C. Gan, W. Cao, C. Li, and S. J. Finney, "Split converter-fed SRM drive for flexible charging in EV/HEV applications," *IEEE Trans. Ind. Electron.*, vol. 62, no. 10, pp. 6085-6095, Oct. 2015.
[39] F. Yi and W. Cai, "Modeling, control, and seamless transition of the bidirectional battery-driven switched reluctance motor/generator drive based on integrated multiport power converter for electric vehicle applications," *IEEE Trans. Power Electron.*, vol. 31, no. 10, pp. 7099-7111, Oct. 2016.
[40] C. Gan, J. Wu, Y. Hu, S. Yang, W. Cao, and J. M. Guerrero, "New integrated multilevel converter for switched reluctance motor drives in plug-in hybrid electric vehicles with flexible energy conversion," *IEEE Trans. Power Electron.*, vol. 32, no. 5, pp. 3754-3766, May 2017.
[41] R. R. Ahrabi, H. Ardi, M. Elmi, and A. Ajami, "A novel step-up multiinput DC-DC converter for hybrid electric vehicles application," *IEEE Trans. Power Electron.*, vol. 32, no. 5, pp. 3549-3561, May 2017.
[42] B. C. Mecrow, J. W. Bennett, A. G. Jack, D. J. Atkinson and A. J. Freeman, "Drive topologies for solar-powered aircraft," *IEEE Trans. Ind. Electron.*, vol. 57, no. 1, pp. 457-464, Jan. 2010.
[43] M. Abdelhamid, R. Singh, A. Qattawi, M. Omar and I. Haque, "Evaluation of on-board photovoltaic modules options for electric vehicles," *IEEE J. Photovoltaics*, vol. 4, no. 6, pp. 1576-1584, Nov. 2014.
[44] A. Diab-Marzouk and O. Trescases, "SiC-based bidirectional cuk converter with differential power processing and MPPT for a solar powered aircraft," *IEEE Trans. Transport. Electrific.*, vol. 1, no. 4, pp. 369-381, Dec. 2015.
[45] Y. Hu, C. Gan, W. Cao, Y. Fang, S. J. Finney, and J. Wu, "Solar PV-powered SRM drive for EVs with flexible energy control functions," *IEEE Trans. Ind. Appl.*, vol. 52, no. 4, pp. 3357-3366, Jul./Aug. 2016.
[46] J. H. Park, B. H. Cho, "Small signal modeling of hysteretic current mode control using the PWM switch model," *IEEE Workshops on Computers in Power Electronics*, Troy, USA, 2006, pp. 225-230.
[47] T. J. E. Miller, *Switched Reluctance Motors and Their Control*. Hillsboro, OH, USA: Magna Physics Pub., 1993.
[48] R. Krishnan, *Switched Reluctance Motor Drives: Modeling, Simulation, Analysis, Design and Applications*, Boca Raton, FL, USA: CRC Press, Jun. 2001.
[49] W. Cai and F. Yi, "An integrated multiport power converter with small capacitance requirement for switched reluctance motor drive," *IEEE Trans. Power Electron.*, vol. 31, no. 4, pp. 3016-3026, Apr. 2016.
[50] J. Y. Chai, Y. C. Chang and C. M. Liaw, "On the switched-reluctance motor drive with three-phase single-switch switch-mode rectifier front-end," *IEEE Trans. Power Electron.*, vol. 25, no. 5, pp. 1135-1148, May 2010.
[51] H. N. Huang, K. W. Hu, Y. W. Wu, T. L. Jong and C. M. Liaw, "A current control scheme with back EMF cancellation and tracking error adapted commutation shift for switched-reluctance motor drive," *IEEE Trans. Ind. Electron.*, vol. 63, no. 12, pp. 7381-7392, Dec. 2016.

**Chun Gan** (S'14–M'16) received the B.S. and M.S. degrees in power electronics and motor drives from China University of Mining and Technology, Jiangsu, China, in 2009 and 2012, respectively, and the Ph.D. degree in power electronics and motor drives from Zhejiang University, Hangzhou, China, in 2016.

He is currently a Research Associate with the Department of Electrical Engineering and Computer Science, University of Tennessee, Knoxville, TN, USA. He is also a Research Staff of the U.S. Energy/National Science Foundation cofunded Engineering Research Center CURENT. He has published more than 50 technical papers in leading journals and conference proceedings, including more than 20 IEEE Transaction papers, and authored one book chapter. He has twelve issued/published invention patents. His research interests include high-efficiency power converters, electric vehicles, electrical motor drives, electrical motor design, continuous variable series reactors, high-voltage direct current transmission, and microgrids.

Dr. Gan received the 2015 Top Ten Excellent Scholar Award, the 2016 Excellent Ph.D. Graduate Award, the 2015 Ph.D. National Scholarship, the 2015 Wang Guosong Scholarship, and the 2014 and 2015 Outstanding Ph.D. Candidate Awards in Zhejiang University.

**Nan Jin** (M'16) received the B.S. and M.S. degrees in electrical engineering from Zhengzhou University of Light Industry, Zhengzhou, China, in 2003 and 2007, respectively, and Ph.D. degree in power electronics and electrical drives from Shanghai Jiao Tong University, Shanghai, China, in 2012.

He is an associate professor in Zhengzhou University of Light Industry, Zhengzhou, China. He is currently a visiting professor with the Department of Electrical Engineering and Computer Science, The University of Tennessee, Knoxville, TN, USA. He has published more than 30 technical papers in journals and conference proceedings, two books and hold 8 Chinese patents. His research interests include model predictive control method for power converter, fault diagnosis and tolerant control of power electronics system.

**Qingguo Sun** received the B.S. degree in Electrical Engineering from Qingdao University, Shandong, China, in 2014. He is currently working toward Ph.D. degree at the College of Electrical Engineering, Zhejiang University, Hangzhou, China.

His research interests include motor design and control in switched reluctance motor, particularly for the optimization of the torque ripple and efficiency of the motor system.

**Wubin Kong** (M'15) was born in Zhejiang, China, in 1986. He received the B.S. and Ph.D. degree from Zhejiang University, Hangzhou, China in 2009 and 2014, respectively. His research interests are high-power multiphase motor drives and fault tolerant control motor drive applied in EV. From 2015, he has been a lecture with Huazhong University of Science and Technology, Wuhan, China.

**Yihua Hu** (M'13-SM'15) received the B.S. degree in electrical motor drives in 2003, and the Ph.D. degree in power electronics and drives in 2011, both from China University of Mining and Technology, Jiangsu, China.

Between 2011 and 2013, he was with the College of Electrical Engineering, Zhejiang University as a Postdoctoral Fellow. Between November 2012 and February 2013, he was an academic visiting scholar with the School of Electrical and Electronic Engineering, Newcastle University, Newcastle upon Tyne, UK. Between 2013 and 2015, he worked as a Research Associate at the power electronics and motor drive group, the University of Strathclyde. Currently, he is a Lecturer at the Department of Electrical Engineering and Electronics, University of Liverpool. He has published more than 35 peer reviewed technical papers in leading journals. His research interests include PV generation system, power electronics converters and control, and electrical motor drives.

**Leon M. Tolbert** (S'88–M'91–SM'98–F'13) received the bachelor's, M.S., and Ph.D. degrees in electrical engineering from the Georgia Institute of Technology, Atlanta, GA, USA, in 1989, 1991, and 1999, respectively.

He was with Oak Ridge National Laboratory, Oak Ridge, TN, from 1991 until 1999. He was appointed as an Assistant Professor in the Department of Electrical and Computer Engineering, The University of Tennessee, Knoxville, TN, USA, in 1999. He is currently the Min H. Kao Professor and the Department Head in Electrical Engineering and Computer Science, The University of Tennessee. He is a founding member of the National Science Foundation/Department of Energy Research Center, Center for Ultra-Wide-Area Resilient Electric Energy Transmission Networks. He is also a part-time Senior Research Engineer in the Power Electronics and Electric Machinery Research Center, Oak Ridge National Laboratory. In 2010, he was a Visiting Professor with Zhejiang University, Hangzhou, China.

Prof. Tolbert is a Registered Professional Engineer in the State of Tennessee. He received the 2001 IEEE Industry Applications Society Outstanding Young Member Award, and six Prize Paper Awards from the IEEE Industry Applications Society and the IEEE Power Electronics Society. From 2003 to 2006, he was the Chairman of the Education Activities Committee of the IEEE Power Electronics Society and an Associate Editor for the IEEE POWER ELECTRONICS LETTERS. He was an Associate Editor for the IEEE TRANSACTIONS ON POWER ELECTRONICS from 2007 to 2013. He was elected to serve as a Member-At-Large to the IEEE Power Electronics Society Advisory Committee for 2010–2012, the Chair of the PELS Membership Committee from 2011 to 2012, and a member of the PELS Nominations Committee from 2012 to 2014. He is currently the Paper Review Chair for the Industrial Power Converter Committee of the IEEE Industry Applications Society.